

Integration of artificial neural network with finite element analysis for residual stress prediction of direct metal deposition process

F. Hajializadeh, A. Ince *

Department of Mechanical, Industrial, and Aerospace Engineering, Concordia University, Montreal, QC, H3G 1M8, Canada



ARTICLE INFO

Keywords:

Additive manufacturing
Direct metal deposition
Residual stress
Machine learning
Neural network
Finite element analysis

ABSTRACT

Direct Metal Deposition (DMD) process is considered to be an efficient and reliable manufacturing method for the production of complex parts in many design applications. The thermo-mechanical nature of the DMD process induces a significant amount of residual stresses and distortions on fabricated parts. Evaluation of residual stress distributions requires considerable amount of modeling and experimental works. Therefore, there is a need for an accurate, and feasible assessment method(s) for engineers to estimate residual stresses based on chosen process parameters and geometrical features of DMD built parts. A novel artificial neural network-based modelling approach integrated with finite element analysis is proposed to address shortcomings of conventional thermo-mechanical finite element-based models and improve the computational efficiency of predicting residual stresses of AISI 304 L parts built on the basis of the DMD process. Predicted results showed that the novel approach is capable of accurate and efficient prediction of residual stress distributions of three different geometric structures e.g. a plane wall shape, L-shape wall, and rectangular box structures. Furthermore, the computational time of predicting the residual stresses for the wall, L-shape wall, and rectangular box structures is significantly improved with respect to the classical finite element thermo-mechanical analysis.

1. Introduction

Additive manufacturing (AM) process has recently achieved considerable interest in academia and industrial applications [1–7]. AM processes refer to fabrication of parts in an incremental and layer-by-layer deposition by utilizing a thermal heat source to melt a feeding powder or wire into the melt pool and its solidification on a substrate or previous layer [8,9]. The design procedure for a complex part with non-symmetric shape and arbitrary geometrical features requires lots of small and basic alterations, both on the geometry of parts and process parameters, to reach the most optimized production procedure. Therefore, production methods need to be completely flexible and capable of applying all changes to designed parts. The conventional production methods are severely restricted to the shape and features of the designed component. In other words, the conventional fabrication methods require considerable modifications in the machinery and tooling to be capable of fabricating complex-shaped parts after the alterations considered in every design step. The slightest changes in the geometry of the final product design could result in considerable time and cost in machinery and tooling modifications. Hence, acquiring a

certain fabrication procedure to handle all the small alterations in the geometry and material of the final product is essential. AM processes were recently introduced to overcome all those shortcomings and difficulties. In a typical AM process, a heat source is mounted on a computer numerical control (CNC) machine. The part geometry in the form of a computer aided design (CAD) file is converted into sequences of the thermal heat source motions and fed into the CNC machine. Therefore, the generation of scanning paths for the heat source motion for any given geometrical shape is feasible. AM processes are known as cost-effective, time-efficient, and well-adaptive production methods that enable engineers/designers to develop more realistic and comprehensive designs. The process that was primarily known as the rapid prototyping method, has been evolved into a small-batch production method due to its high potential in the fabrication of complex-shaped components and great compatibility with different materials such as metal alloys, plastics, and ceramics [10–12].

As the heat source moves during a typical deposition of a metal alloy in direct metal deposition (DMD) process, a material point of interest experiences steep and irregular thermal gradient cycles which result in sudden the material expansion and contraction. The newly solidified material is cooled down immediately and shrinks thus imposing tensile

* Corresponding author.

E-mail address: ayhan.ince@concordia.ca (A. Ince).

Nomenclature	
AM	Additive manufacturing
CAD	Computer-aided design
FE	Finite elements
ML	Machine learning
\bar{X}	Spatial coordinates vector
t	Time
Q	Body heat source
ρ	Material density
C_p	Specific heat of material
k	Conductivity
T	Temperature
σ	2nd order Cauchy stress tensor
b	Body force vector
ε^e	Elastic strain
ε^{th}	Thermal strain
λ	Plastic multiplier
κ	Current yield stress
σ_s	Deviatoric stress
σ_m	Hydrostatic stress
μ	Lame's coefficient
\vec{w}	Weights in ANN
\emptyset	Activation function
$ReLU$	Rectified linear unit
g	Loss function
\vec{s}	Optimal step direction in backpropagation algorithm
S_{12}, S_{13}, S_{23}	Shear components of stress
CNC	Computer numerical control
DMD	Direct metal deposition
ANN	Artificial neural networks
CFD	Computational fluid dynamics
q^p	Total temperature-dependent heat flux flows
P	Heat source power
η	Efficiency of the heat source
x, y, z	Coordinates of elements
a_b, b_b, c_b	X, Y, Z Length of ellipsoid in longitudinal, depth, and transverse directions
v	Transverse speed of the heat source
h	Convection coefficient
T_∞	Ambient temperatures
ϑ	Emissivity
Φ	Stefan-Boltzmann constant
ε	Total strain
ε^p	Plastic strain
C	4th order temperature-dependent stiffness tensor
f	Yield function
α	Back stress
\hat{n}	Flow direction
H	Hardening value
z_N	Net input of the neuron
\vec{x}	Input vector in ANN
Y_b	Scaled distance from the substrate
MSE	Mean squared error
S_{11}, S_{22}, S_{33}	Stresses in the X, Y and Z directions

stresses on the previously deposited material. Strains in the longitudinal direction are gradually changing from compressive to tensile as the heat source moves away from the deposited material and the deposited material is cooled down to the room temperature. These sequences are repeated for every point of interest in the built component. However, the magnitude of tensile residual stresses is reduced as upper layers are deposited [13]. The presence of residual tensile stresses inside a medium is not beneficial from fatigue strength and corrosion resistance perspectives. On the other hand, tensile residual stresses are formed between the newly deposited layer and the substrate or lower layers in the

stacking direction. Moreover, the magnitude of the residual stresses decreases and gradually transforms into compressive residual stresses as the deposition of upper layers continues. The thermal expansion of built layers beneath the heat source induces compressive stresses in the lower layers and thus resulting in compressive plastic strains [14]. The main concern is related to the tensile residual stresses between the newly deposited layer and its substrate as it acts as a driving force for delamination of the built component [14]. As well-known, the formation of residual stresses is inevitable throughout the DMD process. A vast range of parameters e.g. process parameters, material properties and boundary

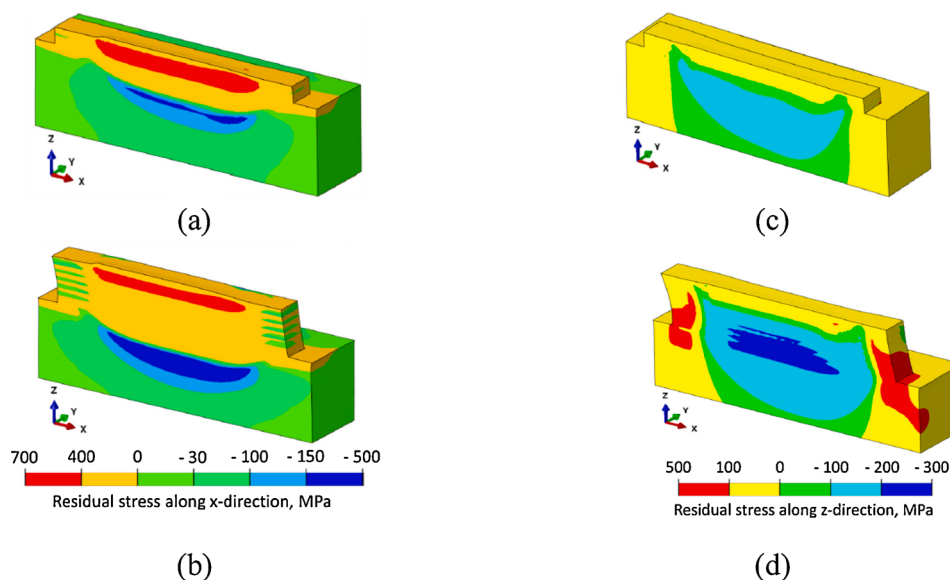


Fig. 1. Formation of residual stresses in the longitudinal direction (a) 2nd layer, (b) 6th layer, and stacking direction (c) 2nd layer, (d) 6th layer [14].

conditions of the built part have a significant impact on the distribution and magnitude of the residual stresses in the AM part. Therefore, understanding effects of all those factors on distortion and residual stress behaviors of built parts is essential in order to effectively employ the potential of the AM process as viable fabrication process for fabricating structural components in many different industries (Fig. 1).

Finite element (FE) analysis appears a powerful numerical method that can be utilized to predict complex mechanical behavior of structures in engineering applications [15,16]. FE models on the basis of thermo-mechanical analysis have been extensively developed to determine the residual stress distribution in welded joints [17–19]. In recent years, FE numerical analyses have been increasingly adopted to predict and simulate residual stresses and geometrical distortions of AM products [20,21]. It is evident that the numerical based models can provide useful information for estimating the residual stress distribution during deposition and after completion of the workpiece built with AM processes. However, reliable responses are strongly dependent on the realistic introduction of all applicable process parameters and material properties used in finite element-based numerical models [14]. Considering all the parameters with actual characteristics of a thermo-mechanical process is not practically possible and some simplifying assumptions are made to develop finite element (FE)-based models [22]. On the other hand, the FE-based models for complex-shaped structures require high computational time which is not efficient in terms of cost and time perspective to predict the distribution of residual stresses and distortions. Therefore, researchers have attempted to boost up the computational efficiency by introducing different modeling techniques coupled with FE analysis. A mesh coarsening approach was developed to improve the computational time of the FE analysis by reducing the total degrees of freedom for FE models [23]. The Mesh coarsening approach is based on the concept that thermal gradients decrease for lower deposited layers as the heat source moves away. Therefore, those layers can be meshed with larger mesh sizes as the effects of thermal gradients diminish in order to reduce total degrees of freedom for the FE model of the fabricated part. Hajializadeh and Ince [23] presented the FE-based mesh coarsening method for performing both thermal and mechanical analyses to reduce the computational time of an AISI 304 L L-shape part fabricated by the DMD process. Jayanath and Achuthan [22] reported a similar mesh coarsening technique based on ABAQUS solution map method. In addition to adaptive mesh coarsening approaches to reduce computational time, some researchers [13, 24–26] utilized a concept of inherent strain developed by Udea [27] to predict distortion of welded structures. The inherent strain method is based on the hypothesis that the plastic strain yields incompatibility in the welded structure thus resulting in the part distortion. In order to employ the inherent strain method for modeling of AM process, the thermo-mechanical FE analysis is performed first so that the inherent strains can be determined. After components of the inherent strain are obtained, they are used as orthotropic thermal expansion coefficients in commercial FE packages. Afterward, the temperature of the model is enhanced by unity so that the inherent strains are applied on the part [13]. Keller and Ploshikhin [24] suggested the idea of a mechanical equivalent layer on the basis of dividing the model into micro, meso, and macro scales. The authors reported good agreement between the experimental data and the predicted results.

Recently, some researchers focused on implementing the concept of machine learning (ML) in the context of solid mechanics [28–34]. Artificial neural networks (ANN) are among the most common machine learning algorithms that have been widely used in many different applications. Koeppe et al. [29] combined the FE analysis, experiment, and ANNs to predict stress of parts made from polylactic acid. The authors generated 85 sets of linear elastic-plastic FE models of lattice-cell specimens with different loading conditions to build training and testing datasets for the ANN model. The trained ANN model was used to make predictions of given loading conditions. The ANN model showed good agreement with FE models and provided a substantial reduction in

the computational time. Liang et al. [30] integrated ML algorithms with computational fluid dynamics (CFD) models of human Aorta to predict the wall stress of the Aorta for different patients. Based on advanced image decoding techniques, e.g. principal component analysis (PCA), they derived different shapes and characteristics of 729 patients and ran the simulations to generate the comprehensive training and testing dataset. The error of 0.492 % in Aorta's wall stress distribution was reported with a significant reduction in the computational time. Gulikers [31] established a method of integrating FE analysis with ANNs to find an effective and reliable solution for the homogenization of complex and inhomogeneous substructures such as airplane fuselage. The FE analysis has been used to generate detailed substructure models and building the training dataset considering elastic-plastic analysis with varying loading conditions and different strain/stress increments. The ANNs with the feed-forward scheme were used and trained with the generated data. Then, the trained network was implemented in the UMAT subroutine in the Abaqus FE package to substitute the elasticity equations for determination of strain and stress and replace the inhomogeneous substructure with a homogenized equivalent element. It was concluded that integrating the FE analysis with ANNs reduced the complexity of the fuselage structure and the computational time of predicting stresses under different loading conditions. Chowdhury and Anand [32] presented a new modeling framework based on ANNs to compensate for the geometrical distortions of AM parts during the design step. The authors used a feed-forward ANN with a back-propagation algorithm to train the network. By varying the process parameters and measuring the geometrical and dimensional deviations from the CAD file, they built the dataset for the training purpose. Afterward, the trained network was used to calculate to predict the distortions based on the input process parameters and compensate for the geometrical accuracy of the part. Li et al. [33] implemented the machine learning concept to estimate the surface roughness of AM parts. The authors built the training data set based on the temperature and vibration data points on the structure. High accuracy of surface roughness prediction was reported by the authors. Mortazavi and Ince [34] developed a machine learning-based fatigue damage prediction method using radial bases function ANN to predict the fatigue crack growth rate for both short and long cracks. The authors used various experimental data sets to train the network and used it to predict the complex crack growth rate of Ti-6Al-4 V, 2024-T3, and 7075-T6 alloys. It was shown that the proposed model was capable of predicting the complex crack growth behavior of both long and short cracks. However, for the cases with limited data set especially for short cracks, the authors reported that the model was unable to accurately estimate the crack growth behavior. To the best knowledge of the current authors, all present research works conducted so far has mainly focused on using the trained ANNs to predict stresses/strains of components that are very similar to the original components used for generating the training data. In most cases, only the process parameters such as loading conditions are varied to build the training dataset and the other parameters including the geometry and boundary conditions remain constant or very slightly varied over different experiment/simulation setups.

In the present study, a novel modeling approach of integrating ANN algorithms with FE analysis is proposed to predict residual stress distributions of structural parts (i.e. a plane wall shape, L-shape wall, and rectangular box structures) fabricated by the DMD process. The training dataset is generated from the FE analysis of 12 layers structural parts and used to train the ANNs. Then, the residual stress distributions of 18 layers parts are predicted using the trained network model. The proposed modeling approach can be utilized in investigating effects of process parameters in future research studies to evaluate their impacts on the residual stress distribution of AM parts in an efficient and effective framework without the need to perform computationally intensive thermo-mechanical non-linear FE analysis. The integrated ANN-FE modeling approach enables a computationally-efficient innovative simulation tool for predicting post-AM residual stresses. The modeling

framework allows us to investigate optimized AM process parameters to minimize resulting residual stresses and distortions of complex geometrical structures before the fabrication process. Thus, the modeling approach leads to widen design applications of the AM products in critical load bearing conditions.

2. Finite elements analysis of direct metal deposition process

The FE analysis of the DMD process comprises the thermal and mechanical analyses. Firstly, the non-linear transient heat transfer analysis is carried out based on the temperature-dependent thermal properties and boundary conditions to determine the temperature history of the elements as a pure heat transfer analysis. Then, the temperature histories of the elements are applied to the mechanical analysis to calculate the mechanical response of the part. Analogous to the thermal analysis, the mechanical properties of the material are considered temperature-dependent in the non-linear elasto-plastic analysis. This approach known as the uncoupled approach is recommended in the literature as an efficient and reliable approach for the FE based thermo-mechanical analysis [23]. A schematic flow of the uncoupled approach for the thermo-mechanical analysis of AM process is shown in Fig. 2.

By applying the concept of energy conservation on a medium and using the non-linear isotropic Fourier heat flux constitutive model, the partial differential equation that leads to the determination of the nodal temperatures can be expressed in Eq. (1) [35–40]:

$$Q(\bar{\mathbf{X}}, t) - \rho C_p(T) \frac{dT}{dt} + \nabla \cdot [k(T) \nabla T] = 0 \quad (1)$$

Where $\bar{\mathbf{X}}$ is spatial coordinates, t is time, ρ is material density, C_p is specific heat of material, k is conductivity and T is temperature. Q is the body heat source expressed as the 3D Goldak double ellipsoidal model shown in Fig. 3.

The Goldak double ellipsoid model expressed in Eq. (2) is adapted to simulate the thermal heat source of the DMD process [41].

(Please refer to Fig. 3)

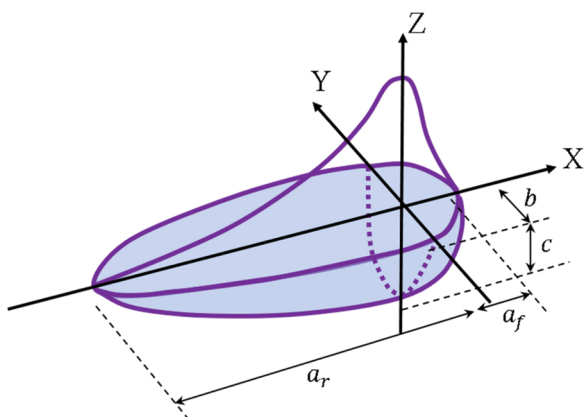


Fig. 3. Goldak double ellipsoidal heat source model.

$$Q(\bar{\mathbf{X}}, t) = \begin{cases} \frac{6\sqrt{3} P f_f \eta}{abc\pi\sqrt{\pi}} e^{-\left(\frac{3(x-vt)^2}{a_f^2} + \frac{3y^2}{b^2} + \frac{3z^2}{c_b^2}\right)} & ; \text{if } x \geq vt \\ \frac{6\sqrt{3} P f_r \eta}{abc\pi\sqrt{\pi}} e^{-\left(\frac{3(x-vt)^2}{a_r^2} + \frac{3y^2}{b^2} + \frac{3z^2}{c_b^2}\right)} & ; \text{if } x < vt \end{cases} \quad (2)$$

Where P is heat source power, η is the beam (laser or electron beam) efficiency, x, y , and z are the coordinates. a_f and a_r are the semi-axes of the beam in the double ellipsoid model in front and rear of the moving heat source.

In order to save computational time, the rear length of the ellipsoid was considered four times of the front length of the ellipsoid ($a_r = 4a_f$) [41]. And, b_b and c_b are the length of the ellipsoid in the transverse and depth directions, respectively. v is the transverse speed of the heat source in the X-direction, and t is the time. f_f and f_r are the fractions of the heat flux acting on the front and rear of the heat source, respectively.

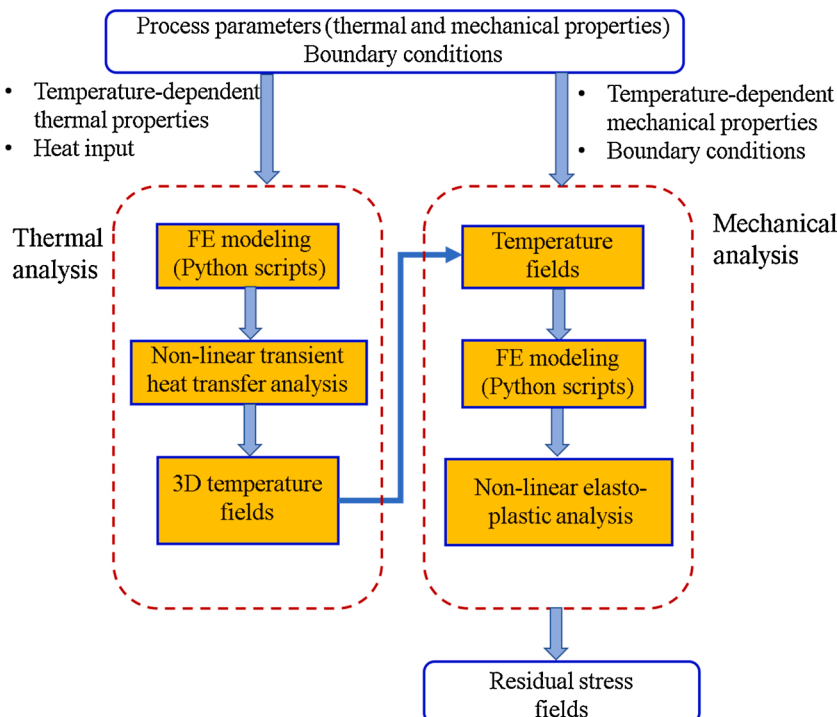


Fig. 2. Schematic flow of uncoupled thermo-mechanical analysis.

Considering the continuity of the volumetric heat source [41,42]:

$$f_f = \frac{2a_f}{a_f + a_r} ; f_r = \frac{2a_r}{a_f + a_r} \quad (3)$$

Effects of the convection and radiation of surfaces are applied as the temperature-dependent boundary condition to solve Eq. (1) using Galerkin finite element discretization and the Newton-Raphson solution. The total temperature-dependent heat flux that flows out of the surface of the part is given in Eq. (4) [37]:

$$q^p = h(T - T_\infty) + \vartheta\Phi(T^4 - T_\infty^4) \quad (4)$$

Where, h is convection coefficient, T and T_∞ are the nodal (surface) and ambient temperatures, respectively, ϑ is emissivity and Φ is the Stefan-Boltzmann constant. It is noted that the material density has not been considered as temperature-dependent as its dependency is negligible with respect to temperature.

Another key factor in FE-based analysis of AM processes is related to the implementation of the thermal source; Q in Eq. (1). Considering the difficulties associated with the thermal source model, some studies [43, 44] adapted simpler models based on Rosenthal [45] melting pool estimation. The Goldak double ellipsoid model has been extensively used in the literature [46]. Although, the main part of the heat transfer phenomenon is carried out by the material conductivity even inside the melt pool, a number of studies which emphasize on the effect of convection heat transfer inside the melt pool [14,47,48]. The research studies [14,47,48] demonstrated over-estimation of the cooling rate in AM processes by disregarding the convective heat transfer inside the melt pool. Very steep thermal gradients exist inside the melt pool which results in the formation of turbulent molten material flow. The material flow inside the melt pool has an impact on heat transfer analysis and the shape of the melt pool. Considering all the important factors responsible for heat transfer phenomena inside of the melt pool, Mukherjee et al. [14] proposed a novel heat source model in the direct energy deposition (DMD) of Ti-6Al-4 V and IN 718 powder. The authors reported very good agreement between experimental and numerical results. Manvatkar et al. [48] introduced a thermal source model by accounting for the convective heat transfer inside the melt pool during DMD of powder SS316 alloy.

The DMD processing parameters are used as input for the Goldak model to simulate the heat source. The thermal analysis is performed on three configurations demonstrated in Fig. 4 using ABAQUS/STANDARD. All three structural parts are 18-layers parts with a thickness of 1 (mm) per layer and with the length (or width) of 15 (mm). In order to account for the element addition and imposing temperature-dependent material

in the FE analysis, the UMATHT subroutine is developed and implemented in conjunction with ABAQUS. A laser heat source with the power of 250 (w), the front semi-axis of 0.5 (mm), and transverse speed of 11.25 (mm/s) is used and implemented by DFLUX subroutine. The hybrid element activation technique [23,49] is adopted to optimize the efficiency of the FE process. All the layers meshed with 5 elements in the thickness direction using linear brick elements (C3D8T) to ensure that the developed FE model is capable of handling high thermal gradients. The material properties of AISI 304 L are given in Table 1. Furthermore, a constant material density of 7800 (kgm^{-3}) is used for AISI 304 L in the FE analysis.

2.1. Mechanical analysis

After performing the heat transfer analysis and acquiring the nodal temperature history, the structural/mechanical model is constructed to determine the mechanical response of the built part on the basis of the quasi-static analysis. The mechanical analysis is based on the equilibrium condition of a continuum body expressed in Eq. (5) [35,38,50,51]:

$$\nabla \cdot \sigma + b = 0 \quad (5)$$

Where σ is a 2nd order Cauchy stress tensor, and b is the body force vector.

By implementing Hook's law the Cauchy stress can be expressed in Eq. (6) [40]:

$$\sigma = C\epsilon^e \quad (6)$$

Table 1
Thermal and mechanical properties of AISI 304 L [16].

Temperature (°C)	Specific Heat (J/Kg°C)	Conductivity (J/m°C)	Thermal Expansion ($\times 10^{-5}/\text{°C}$)	Yield Stress (MPa)	Young's Modulus (GPa)
20	462	14.6	1.70	319	198.5
100	496	15.1	1.74	279	193
200	512	16.1	1.80	238	185
300	525	17.9	1.86	217	176
400	540	18.0	1.91	198	167
600	577	20.8	1.96	177	159
800	604	23.9	2.02	112	151
1200	676	32.2	2.07	32	60
1300	692	33.7	2.11	19	20
1480	700	120	2.16	8	10

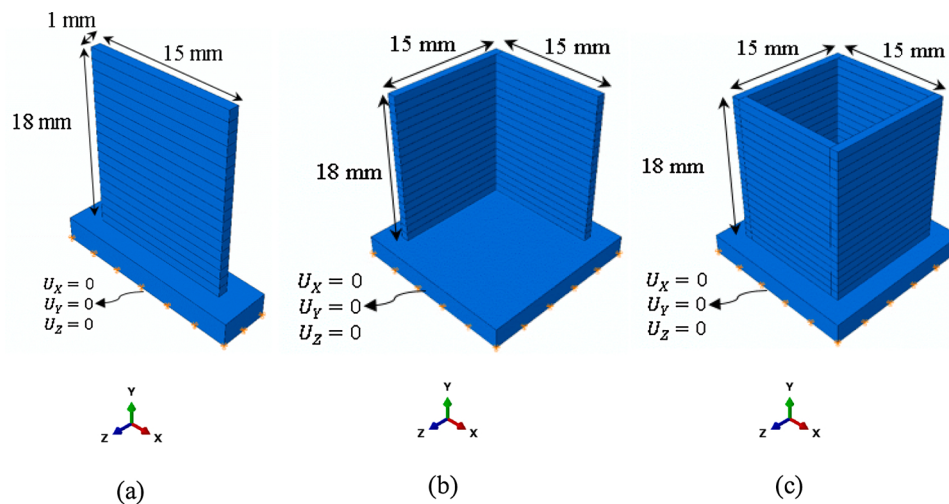


Fig. 4. Three geometries (a) wall, (b) L-shape wall, and (c) rectangular wall for employing new novel approach of integrating the ANN and FE analysis.

Where C is a 4th order temperature-dependent elastic stiffness tensor.

As small deformation is assumed for the FE-based modeling for AM process, the total strain can be decomposed into three different components in Eq. (7) [40]:

$$\varepsilon^t = \alpha \Delta T \quad (7)$$

Where ε , ε^e , ε^p , and ε^t are total, elastic, plastic and thermal strains, respectively, and α is linear thermal expansion coefficient.

By applying boundary conditions on the mechanical FE model, nodal displacements and stresses are computed using Newton-Raphson iterative scheme. Then, the equivalent stress known as von Misses stress is evaluated to determine either the element has reached the elastic limit or not. The yield stress of metal alloys decreases as the temperature increases. Therefore, a proper temperature-dependent yield criterion and flow rule need to be employed. The flow rule (based on Prandtl and Reuss), yield function for isotropic and kinematic hardening rules and flow direction are defined in Eqs. (8)–(11) respectively [52]:

$$\dot{\varepsilon}^p = \lambda \frac{\partial f}{\partial \sigma} \quad (8)$$

$$f(\sigma, \kappa) = \sqrt{2J_2} - \kappa = 0; \text{ Isotropic hardening} \quad (9)$$

$$f(\sigma, \alpha, \kappa) = \|\xi\| - \kappa = 0, \xi = \sigma_s - \alpha; \text{ Kinematic hardening} \quad (10)$$

$$\hat{n} = \frac{\sigma_s}{\|\sigma_s\|}; \sigma_s = \sigma - \frac{1}{3}\sigma_m \quad (11)$$

Where λ is plastic multiplier, f is the J_2 plasticity yield function, and κ is current yield stress, α is back stress, σ_s is deviatoric stress, \hat{n} is the flow direction, and σ_m is hydrostatic stress. It should be noted that the J_2 refers to the second invariant of stress for a given element/integration point.

By implementing the combined isotropic-kinematic hardening rule, the consistency condition yields the plastic multiplier rate as [52]:

$$\dot{\lambda} = \frac{\partial f}{\partial \sigma} : \dot{\sigma} - H\lambda = 0 \quad (12)$$

$$\lambda = \frac{\hat{n} : \dot{\varepsilon}}{1 + H/2\mu} \quad (13)$$

where H is the hardening value obtained from plastic stress-strain curve and μ is Lame's coefficient. And, the current yield stress and back stress are defined in Eq. (14) [52]:

$$\dot{\kappa} = \frac{\beta H}{1 + H/\mu} \hat{n} : \dot{\varepsilon}; \dot{\alpha} = \frac{(1 - \beta)H}{1 + \frac{H}{2\mu}} (\hat{n} \otimes \hat{n}) : \dot{\varepsilon} \quad (14)$$

Where sign “:” stands for double contraction operation of tensors and \otimes is dyadic multiplication sign that $(a \otimes b)_{ijkl} = a_{ij}b_{kl}$. If $\beta = 1$, only isotropic hardening will be functioning and if $\beta = 0$, only kinematic hardening rule is applied.

As for AM processes, as the material experiences thermal cycles, the material deformation should be able to take into account the Bauschinger effect. While kinematic hardening (Prager hardening) is capable of handling the Bauschinger effect, the isotropic hardening is not. For simplicity, only isotropic hardening is considered in the present study to show the capability of the proposed novel approach in determination of residual stress distribution inside the DMD fabricated parts. The hybrid element activation scheme is implemented by developing a UMAT subroutine. The same mesh size used in the thermal analysis is adopted here in mechanical analysis as well to ensure the consistency of corresponding elements in both thermal and mechanical analyses. Analogous to the thermal analysis, linear brick elements (C3D8) are used to discretize the continuous medium of all the selected structures. The bottoms of the substrates are constrained to avoid rigid body motion of

the modeled parts.

However, the main drawback of implementing the FE analysis for evaluation of residual stress distribution for AM parts is the high computational time for the process simulation. Thus, it is essential to develop an accurate and feasible modeling framework to improve the computational efficiency of the FE method. The proposed integrated ANN-FE framework can provide significant potential to address the shortcoming of the FE analysis.

3. Artificial neural networks modeling

Machine learning can be broadly described as algorithms to extract patterns from a given dataset and determine a logical relationship between given data inputs and output(s). In order to apply such techniques, the first step is to build a dataset. Dataset is referred to as the sequence of numbers as inputs and their corresponding output(s). A dataset should be sufficiently large and well-structured that represents the full characteristics of a problem thoroughly. Therefore, the FE analysis is adopted as the appropriate analysis tool for generating sufficient datasets in the present study. Artificial neural networks (ANN) are known as the most popular and powerful machine learning techniques that have been extensively used in different disciplines such as image recognition, financial markets, and weather forecasting. Roseblatt [53] presented a multi-layer artificial neuron that consisted of two mathematical operators as expressed in Eq. (15). The net input of the neuron and an activation function ϕ , is schematically shown in Fig. 5.

$$z_N = \vec{w}^T \vec{x} + b_i \quad (15)$$

The ANN model can consist of several layers and a specific number of neurons in each layer. All the inputs are set in the input layer and the outputs are set in the output layer of the ANN. The ANN can contain one or multiple hidden layers with a predetermined number of neurons. Fig. 5 shows the four layers ANN with two hidden layers used for the construction of the ANN in the present novel approach described in Section 4. A high-level neural network application programming interface (API) developed by Keras [54] is adopted. Implementing Keras API facilitates the construction and modification of the ANN and guarantees high-performance calculations using parallel computation. The input layer/vector of the proposed ANN model consists of elements' temperature history and spatial coordinates and the output layer includes the stress components of the element as shown in Fig. 6. T_1, T_2, \dots, T_f are the temperature history of the elements and X, Y , and Z are the spatial coordinates of the elements according to Fig. 4 and Y_b is the scaled distance from the substrate. N represents the neuron in each hidden layer and its superscript and subscript show the hidden layers number and neuron number, respectively. Each hidden layer may have different neurons as indicated by i and j ; i is the index of the first hidden layers and j is the index of the second hidden layer. The outputs are stress components; S_{11} represents the stress in the X-direction, S_{22} stands for the stress in the stacking direction (or Y-direction), and S_{33} shows the stress in the Z-direction. S_{12}, S_{13} , and S_{23} are the shear stress components.

The mathematical formulation of the implemented ANN for the current study can be presented in Eq. (16).

$$S_{kl} = \sum_{m=1}^6 w_{m,j} \text{ReLU} \left(\sum_{p=1}^j w_{p,i} \text{ReLU} \left(\sum_{r=1}^i w_{r,n} \vec{X}_n + b_r \right) + b_p \right) + b_m$$

$$\text{ReLU}(X) = \begin{cases} x & x > 0 \\ 0 & x \leq 0 \end{cases} \quad (16)$$

$$\vec{X} = \{ T_1 \ T_2 \ T_3 \ \dots \ T_f \ X \ Y \ Z \ Y_b \}^T$$

Where, S_{kl} ($k, l = 1, 2, 3$) are the stress components as the outputs of the network, w and b represent the weights and biases corresponding to each neuron in each layer. The indices n, i , and j are the length of the input

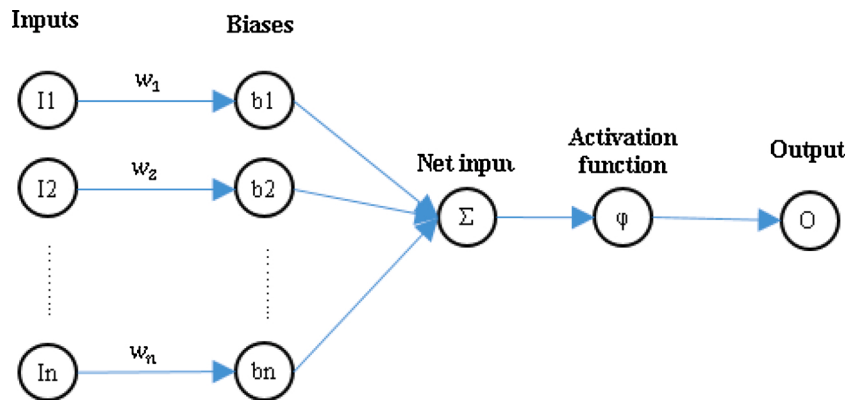


Fig. 5. Layout of ANN structure.

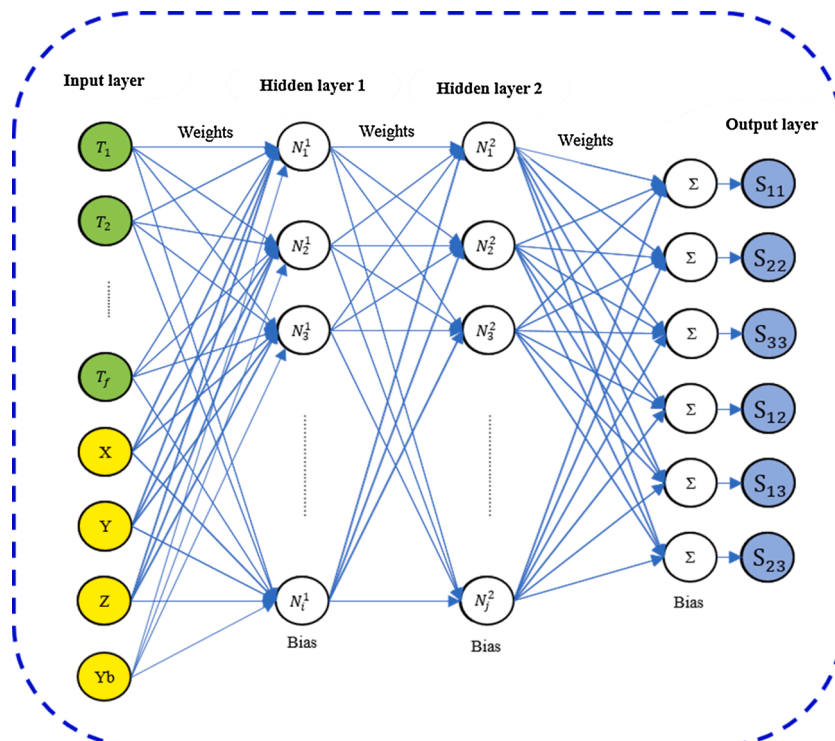


Fig. 6. Multilayer ANN configuration with two hidden layers for the present study.

vector \vec{X} , number of neurons in the first hidden layer layer, and number of neurons in the second hidden layer, respectively. *ReLU* (rectified linear unit) is a non-linear activation function defined for each layer to decide whether the neurons remain in-active or become active.

At first, initial values for weights and biases are considered. By feeding the input vector of data into the network, the stress outputs are evaluated. Because the calculated stresses are different from actual stress values, an error function (e.g. mean squared error) can be established for measuring the deviations. Afterward, the network is trained by adjusting the weights and biases to minimize the error function.

Some parameters such as a number of hidden layers, number of neurons in each layer, activation function in each layer, loss function, number of epochs, and a certain method for optimizing the weights and biases are selected by the user in order to establish an ANN. Features of the ANN model implemented in the training step for all the three structures shown in Fig. 4 are as follow:

Number of hidden layers and also neurons in each layer depend on the size of the input dataset and level of the nonlinearity and complexity

of the dataset. In order to have higher training accuracy and accurate predictions, the number of the hidden layers and the neurons in each layer has to be adjusted in such a way that the network is capable of acknowledging the effect of each input parameter and the possible interplay among them. Nevertheless, by increasing the number of layers and neurons in each layer excessively, the training accuracy could decline. Excessive increase in the number of layers and neurons in each layer results in undermining the effect of each input in the ANN model. For all three structures, only two hidden layers with different number of

Table 2

Number of neurons in the hidden layers of the ANN for the different structures.

Structural part	Number of neurons for the first and the second hidden layer
12-layers wall	2048–1024
12-layers L-shape wall	4096–2048
12-layers rectangular box wall	8196–4096

neurons presented in Table 2 are used;

- ReLU function in the hidden layers and linear function (also called identity) in the output layer are used as the activation functions in the generated network. It is recommended to use a non-linear activation function especially when dealing with non-linear and complex problems [55,56];
- Mean squared error (MSE) is used as the loss function to evaluate the error between the predicted values from the network and the actual output data. The mean squared loss function is the most popular function for regression problems;
- Number of epochs of 1000–2000 epochs are used in the training step for the three structural parts. This value is adjusted based on the training rate of the network and is chosen in such a way that the training accuracy higher than 95 % would be achieved for each of all three structures;

The gradient descent approach with backpropagation is used as an efficient training algorithm [23]. It minimizes the stress prediction error

by finding the local optima of the loss function. The general idea of gradient descent approach is given based on Taylor expansion in Eq. (17) [23]:

$$\vec{s} = \nabla g \text{ as the optimal step direction} \quad (17)$$

Where g represents the loss function (MSE for the developed ANN), p is the step size, and \vec{s} is the derivative of the loss function with respect to the inputs in the network. The derivative of the loss function with respect to any input variable in ANN can be expressed in Eq. (18) [23]:

$$\delta = \frac{\partial g}{\partial z_N} \quad (18)$$

After calculating z_N for every input parameter, the optimal step direction (\vec{s}) is found. Then, based on the reverse computation in the network, starting from the stresses and reaching the temperatures and coordinates of the elements, the weights and biases are modified to minimize the loss function. Thus, the prediction error is minimized. The gradient descent algorithm with back-propagation in ANN is executed on the whole network and the outputs are stored in order to update the weights and biases for the next epoch.

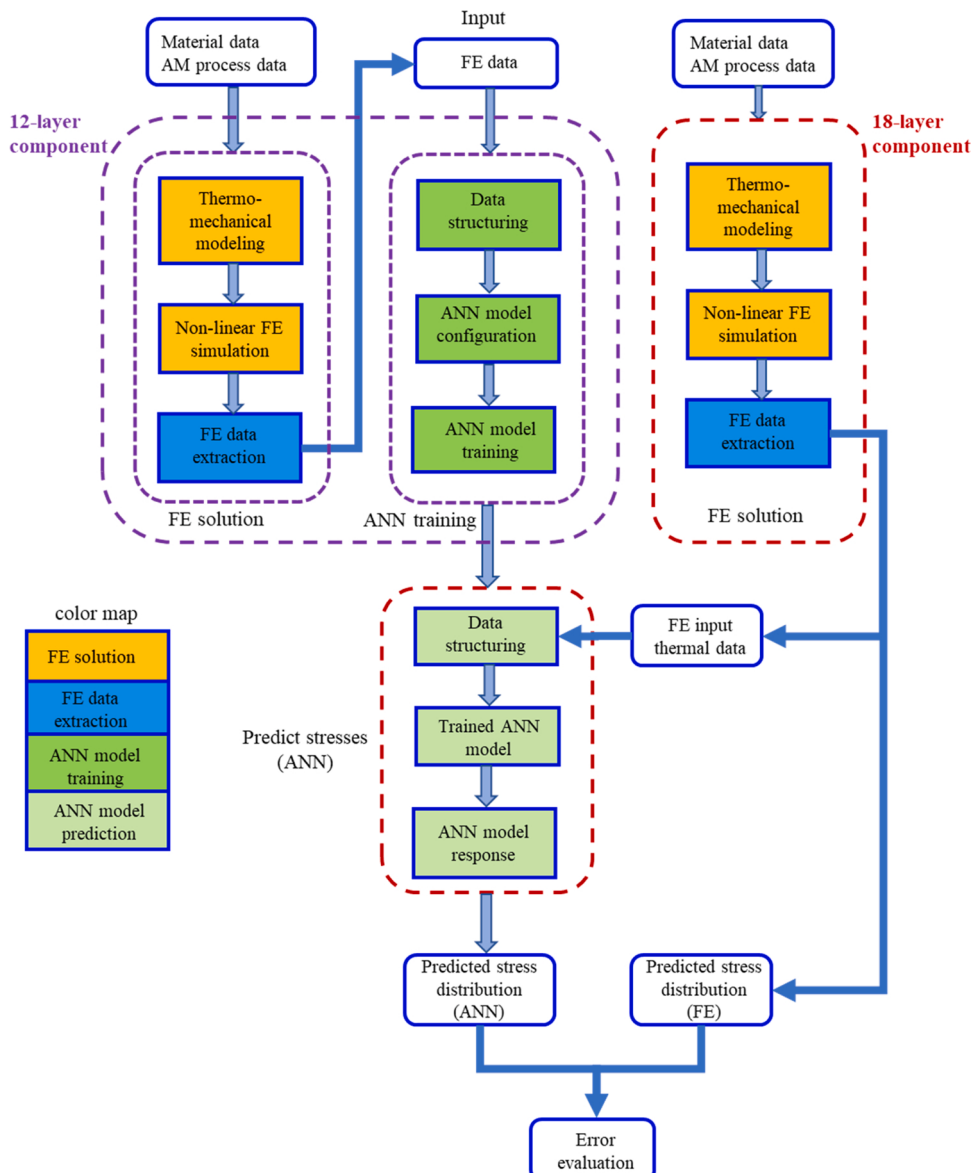


Fig. 7. Schematic algorithm of the novel approach of integrating ANN and FE analysis.

4. Integration of artificial neural networks and finite element analysis

The present study is carried out to use the capabilities of ANN to improve the efficiency of the FE analysis. A schematic representation of the novel approach of integrating the ANN with FE analysis to predict the stress distribution of each AM part is illustrated in Fig. 7. The three simple shapes of AM parts including 18-layers straight wall, L-shape wall, and rectangular box are considered in the present study as illustrated in Fig. 4. For all these geometric structures, the following modeling steps are conducted to develop the proposed integrated ANN-FE framework:

- 1 Detailed thermo-mechanical FE based modeling of the three structural parts is performed using ABQUS commercial package for all three parts with 12 and 18 layers;
- 2 Training and testing datasets are extracted for the both 12 and 18-layers structural parts. The input data include the temperature history of the elements and their spatial coordinates and the output data consist of the stress components for elements of the three structural models;
- 3 The features of the ANN are configured based on the size and structure format of dataset obtained from the 12-layers structure.

Then, the ANN is constructed and trained with the training dataset obtained from the 12-layers part;

- 4 The size of the input dataset for 18-layers structures are restructured to fit the format and size of the trained ANN.
- 5 After restructuring, the temperature history of each element with its spatial coordinates is fed into the trained ANN to predict the stress components of the corresponding element. By comparing the difference between the actual and predicted stress values for each element, the prediction error is evaluated for each element of the FE model.
- 6 Predicted stress results are then plotted in the FE model of each structural part for visualization purposes.

4.1. Artificial neural network training

In order to utilize the neural network, it is essential to build a comprehensive dataset and train the ANN based on that. A schematic representation of the data structure is shown in Fig. 8. For generating the training and the testing dataset, FE analysis with fine-mesh is adopted to perform the thermo-mechanical analysis of DMD deposition of all three different AISI 304 L parts in order to extract nodal temperature history and resultant stress distribution of the medium. A Python script is

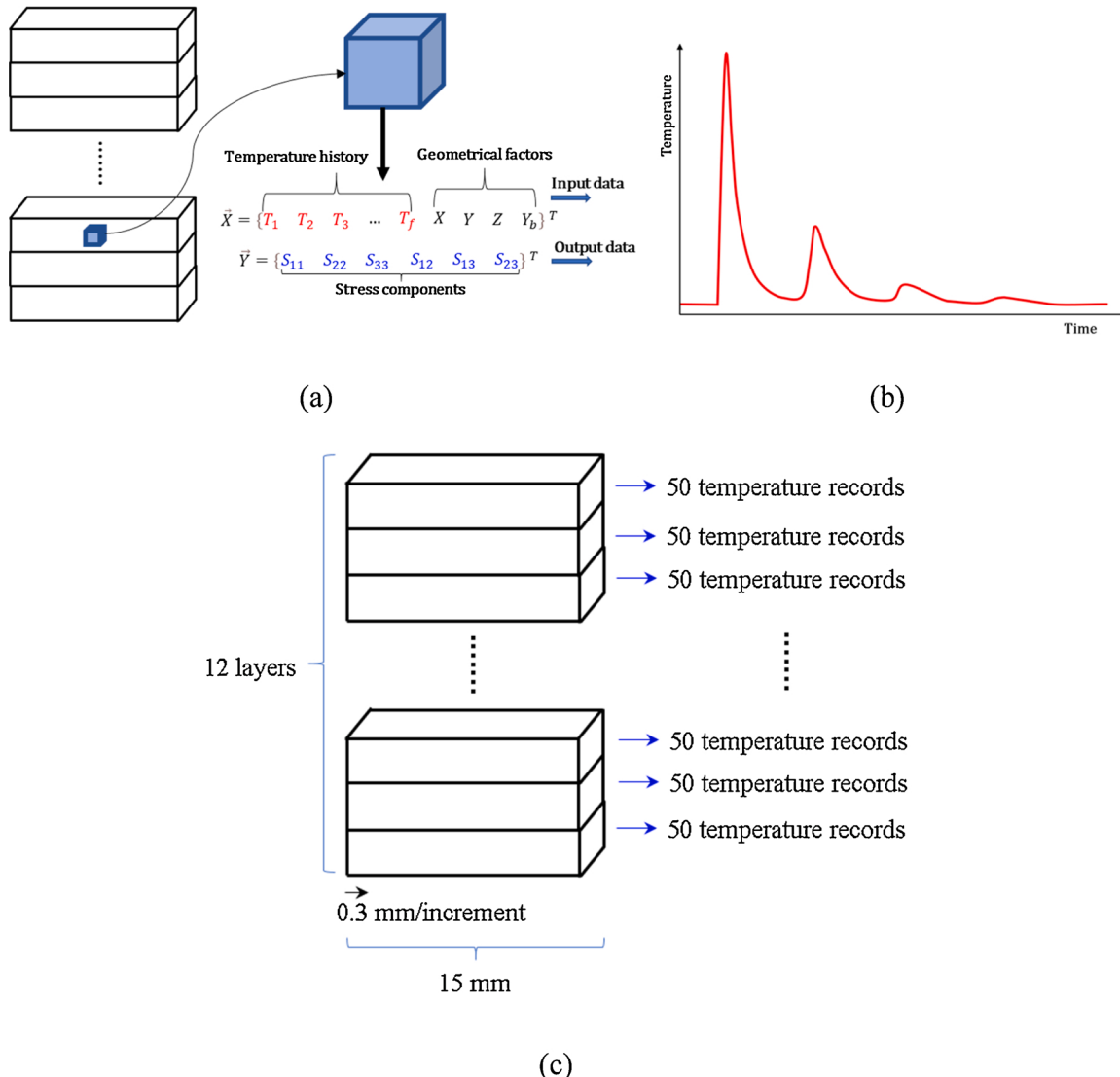


Fig. 8. (a) Input and output data structure (b) temperature history of an element (c) temperature records of 12-layers wall.

developed for the extraction and post-processing of the analysis results. The training dataset is extracted from the thermo-mechanical analysis of 12-layers parts for all three structural parts. Dataset obtained from FE analysis of 12 layers parts demonstrates the capability of representing the physics of the DMD process of AISI 304 L meticulously as it covers all the possibilities of the different temperature history of elements/nodes. The temperature history of elements for three structures are extracted for every 0.3 mm movement of the laser beam. The corresponding time intervals and therefore the input vector size for every element in each structure is determined based on the dimension of the part. Consequently, the temperature history of an element in the 12-layers wall, L-shape, and box parts for each layer will have 50, 100, and 200 temperature records, respectively. Fig. 8 (c) shows the temperature records of every element in the 12-layers wall obtained from depositing each layer. Furthermore, one extra step ($t = 1$ s) was defined in the FE analysis of the 12-layers parts to account for the cooling time of the DED process. Thus, for every element in three structures, 50 extra temperature records are considered to capture the cooling process. Table 3 shows the vector size of the input data extracted from FE analysis for the three structures. For those elements that are not activated in the model i.e. the elements in the second layer and above, the temperature is considered as the room temperature so it would not affect the weights and biases of the ANN.

Fig. 9 shows the schematic representation of training ANN based 12-layers parts. After the training dataset is extracted from the detailed FE analysis of 12-layers structural parts, they are fed into the ANN to perform the training step. According to the training procedure described in section 3, the weights and biases of the ANN are modified in such a way that the prediction error of the network is minimized. For every single epoch, the predicted stresses in the output layer are compared with the exact stresses from FE analysis. If the prediction error is greater than 1%, the next epoch is performed. Once the ANN model is properly trained, it is used for predicting the stress distribution of the elements based on input data of the temperature history of the elements and their spatial coordinates.

4.2. Data restructuring for residual stress predictions

As described in section 3, generating a well-structured and comprehensive dataset is crucial for employing any ANN and performing the proper training step. The data structure is considered as an important factor in any ML algorithm and has a significant impact on the performance of the developed ML algorithm. In the scope of this study, the input data should provide comprehensive features of material deposition in the DMD process. For such problem, the input data are the thermal history and spatial coordinates of the elements/nodes, and the stress/strain distribution and nodal displacements are the outputs. For simplicity, only the stress distribution is considered as the output in this work phase.

According to Fig. 7, after the ANN training is completed, the input dataset for the testing purpose or the model prediction is extracted from the thermal analysis results of 18-layers parts. Since the trained networks for each one of the parts are based on a certain input size, the input data extracted from the 18-layers model should be restructured so that it can be fed into the trained network. Similar to extracting the training data from 12-layers part for training purpose, the dataset for testing purpose is extracted with respect to 0.3 mm of laser movement in the FE analysis. It should be noted that an additional step was defined in the FE analysis of 18-layers parts to account for the cooling of the deposited medium. Therefore, each element in the 18-layers wall, L-

shape and rectangular box will have 950, 1850, and 3650 temperature records. By adding the geometrical factors to the extracted temperature history of the elements, the input vectors of the 18-layers parts are built. However, the input vector sizes of the 18-layers parts are not compatible with the trained ANN. Considering that the ANN is trained based on the 12-layers data for each part, a restructure step is essential to make the input data for 18-layers parts compatible with their corresponding trained ANN. According to Fig. 8 (b), it is evident that after a specific time for any element, the thermal cycles are lumped to a constant temperature. Then, by omitting the additional and constant thermal sequences of the element, the structure of the input data becomes consistent with the trained ANN. The restructuring is demonstrated in Fig. 10 for the 18-layers wall considering an arbitrary element. It should be noted that the restructuring must be executed in such a way that the thermal cycles of the elements would not be affected. Therefore, a Python script is developed in order to change the structure of the input data for every element in each layer.

Except for the elements in the first layer, the elements in the other layers are constrained to take the effect of the previous layer deposition. For instance, for the extraction of the thermal history of an element in the third layer in the 18-layers wall, the thermal history of the element during deposition of the second layer is also included. However, because the element in the third layer would not exist when the second layer was deposited, the thermal history of the element in the third layer is put to room temperature during the timespan of the second layer deposition. Finally, after the input datasets of all the three structural parts are extracted, they are fed into the corresponding trained network for each of the structures and prediction of the stress distribution is accomplished. The error of predicting the residual stress is calculated using the actual data obtained from the thermo-mechanical FE analysis of 18-layers parts.

5. Results and discussion

The proposed modeling approach of integrating ANN and FE-based analysis is developed and verified on three simple parts as shown in Fig. 4. In order to show the capability of the proposed novel method in the prediction of residual stress distribution, the error scatter was calculated using Eq. (19) and presented for each structure. Furthermore, the histogram diagram indicating the percentage of elements having different ranges of the error is provided to exhibit the performance of the proposed approach. For clarification, S_{11} is the stress in the direction 1 (X-direction) and S_{22} is the stress in the direction 2 (Y-direction or the stacking direction). As it is not practically possible to show the prediction error of different stress components for all the elements of the part, only the mid-surface of the FE models was used to demonstrate the error scatter and histogram analysis.

$$Error_{\sigma} = \left| \frac{\sigma_{prediction} - \sigma_{FE}}{\sigma_{prediction}} \right| \quad (19)$$

5.1. 18-layers wall

Fig. 11 shows the S_{11} distribution of the 18-layers wall parts. Fig. 11 (a) and (b) represent the result of the detailed FE analysis and the prediction obtained from the ANN, respectively. Fig. 11 (c) shows the error scatter in 3D spaces and Fig. 11 (d) indicates the histogram analysis of prediction error in the mid-surface of the 18-layers wall. By comparing Fig. 11 (a) and (b), it is evident that the stress distribution pattern of S_{11} across the whole medium is consistent in both cases. The positive residual stress zone at the bottom of the wall where it is connected to the substrate is captured accurately in the novel integrated ANN-FE approach. In the upper layers, the negative S_{11} values predicted using ANN-FE also are in good agreement with the FE results. It is important to note that at the critical locations where S_{11} has its highest magnitude (top layer), the predicted results are very close to the FE results and the

Table 3

Input vector size of the developed ANN for three structures.

Structure	12-layers wall	12-layers L-shape	12-layers box
Input vector size	654 (12 × 50 + 50 + 4)	1254 (12 × 100 + 50 + 4)	2454 (12 × 200 + 50 + 4)

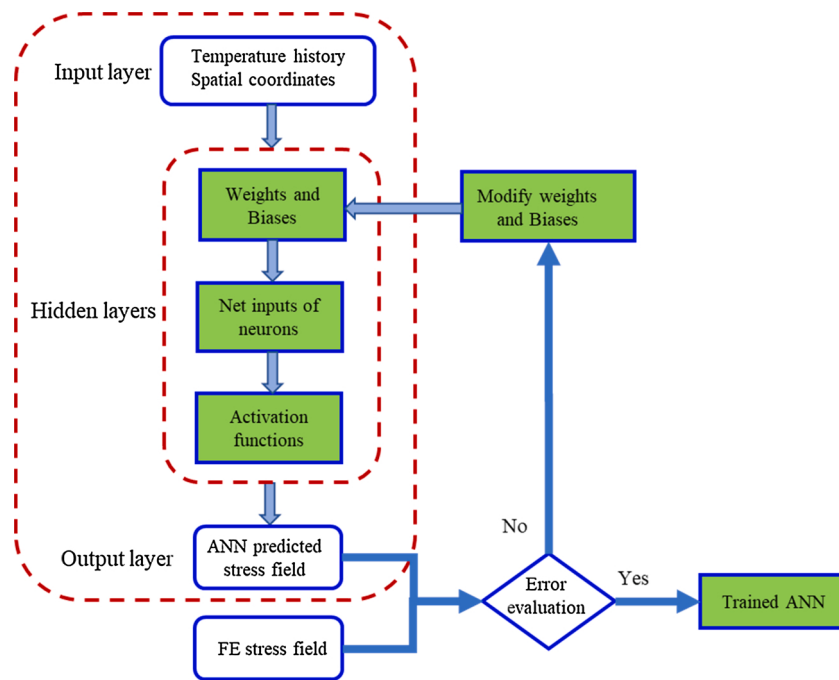


Fig. 9. Schematic of ANN training.

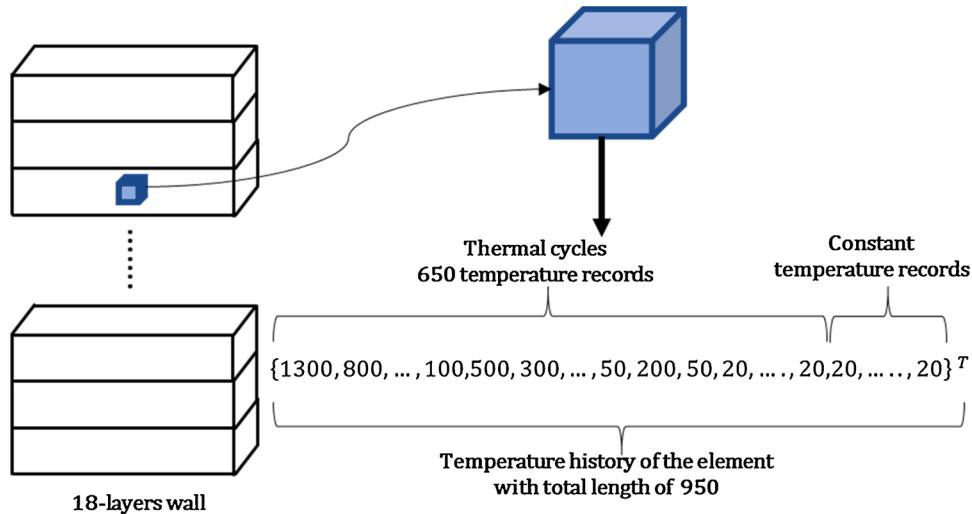


Fig. 10. Restructuring of the input data for 18-layers wall.

error percentage is less than 2 % for that region. A limited number of elements with higher error values indicated in Fig. 11 (c) correspond to the relatively low-stress zone ($S_{11} < 120$ MPa) and it can be considered negligible. The error scatter of S_{11} shown in Fig. 11 (c and d) represents a very limited number of elements that have higher error values than 15 %. This can be clarified by histogram analysis for the error represented in Fig. 11 (d). Approximately 12 % of the elements show the prediction error higher than 15 % and the majority of elements in the higher stress zones, show lower error percentages.

Fig. 12 shows the results of S_{22} (stress component in the stacking direction or along axis 2) distribution over the mid-surface of the 18-layers wall. Fig. 12 (a) and (b) show the results of FE and integrated ANN-FE method, respectively. By comparing the results from the detailed FE analysis and the prediction, it is noted that the overall distribution of S_{22} is consistent in both stress contours. The tensile residual stresses are captured accurately in the both ends of the part by implementing the integrated ANN-FE method. And, high compressive stress

zone is also anticipated meticulously in the middle of the part by using an integrated ANN-FE approach. A very smooth transition from tensile to compressive residual stresses is observed in the predicted results. Top layers of the part show very small residual stresses (approximately -50 to 50 MPa) that is consistent with the FE results. For a better representation of the error, the error scatter is calculated and presented in Fig. 12 (c) in 3D space. The error values are demonstrated in Fig. 12 (c) for the mid-surface of the 18-layers part. It is evident Fig. 12 (c) that the prediction error is low for the majority of the elements. Only a limited number of elements show the error higher than 10 % which is very rare. A large portion of the elements is associated with the red and yellow colors in the scatter diagrams which correspond to an error value of less than 5 %. Less than approximately 9 % of the elements exhibit higher than 10 % error values as shown by the histogram analysis of the error depicted in Fig. 12 (d).

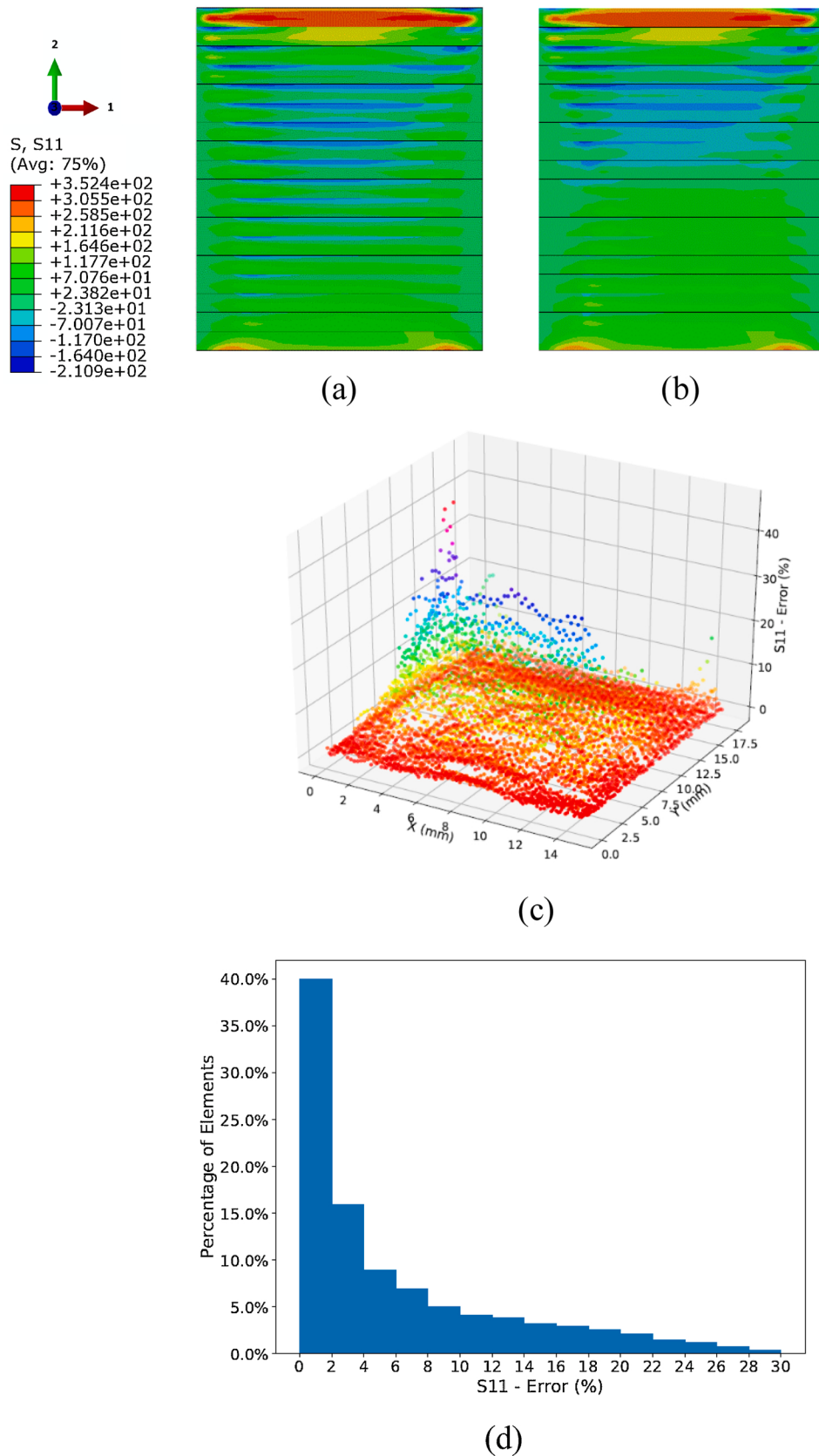


Fig. 11. S_{11} distribution of 18-layers wall (in MPa) (a) FEM analysis (b) integrated ANN-FE (c) 3D error scatter (d) histogram of the error.

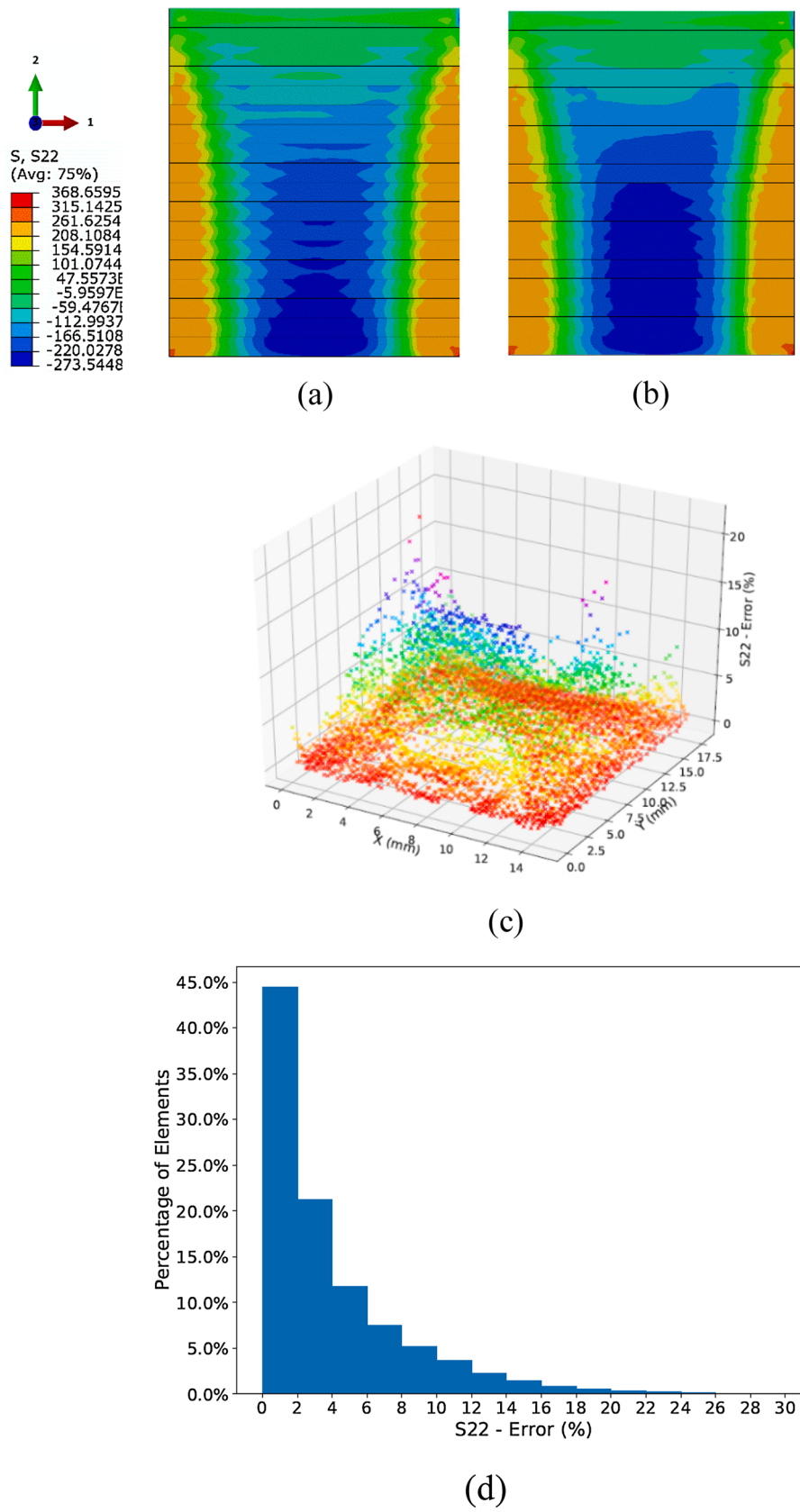


Fig. 12. S_{22} distribution of 18-layers wall (in MPa) (a) FEM analysis (b) integrated ANN-FE (c) 3D error scatter (d) histogram of the error.

5.2. 18-layers L-wall

Fig. 13 shows the S_{11} distribution for the 18 layers L-wall. **Fig. 13** (a) and (b) demonstrate the distribution of S_{11} obtained from the FE analysis and integrated ANN-FE method for the whole medium, respectively. The mid-surface of the right-hand side of the L-wall is cut to show prediction errors in mid plane of the body. On the other hand, the left-hand-side is kept thoroughly to show the stress distribution on the free surface of the medium. By comparing these two contours, it is noticed that the prediction made by the integrated ANN-FE method is consistent with the results from the FE analysis. The highest tensile residual stresses are captured well in the integrated ANN-FE model; the top layer presents very high tensile residual stresses that are smooth in the middle part of the layer. Moreover, the high tensile residual stresses are predicted at the intersection and right end of the L-wall that is consistent with the FE results for S_{11} . Also, the residual stresses are faded at the right end of the medium and at the intersection of the L-wall which is predicted accurately in the integrated ANN-FE model. To further quantify the prediction errors, the error scatter of the elements for the mid-surface of the right-hand side of the L-wall is calculated and shown in **Fig. 13** (c) in 3D space. As it is shown, only a few elements show the highest error which can be neglected. All the red and yellow points on the error scatter diagrams correspond to the error of less than 10 %. Furthermore, the histogram analysis is also performed to analyze the percentage of the elements based on the error ranges in **Fig. 13** (d). Approximately, only 6 % of the elements show error higher than 15 %.

Fig. 14 shows the results for the prediction of S_{22} (stress component in the stacking direction or direction 2) of the mid-surface plane of the right-hand side and the free-surface of the left-hand side of the 18-layers L-wall structure. **Fig. 14** (a) and (b) show the S_{22} distribution in the form of contour obtained from the FE analysis and integrated ANN-FE method, respectively. By comparing the two contours, it is evident that the stress distribution pattern is consistent in both the contours; both ends and the intersection of the L-wall depict the high tensile residual stresses and the middle part of the sides represent highest compressive residual stresses. There is a very smooth transition zone in which the tensile residual stresses are changed into compressive residual stresses. The error evaluation of the predicted results by employing the integrated ANN-FE was performed and the results are shown in **Fig. 14** (c). As it can be seen from **Fig. 14** (c), at the right-hand side of the structure showing the S_{11} error distribution in the mid-surface. **Fig. 14** (c) and (d) show that the very high fraction of elements has a prediction error of less than 10 % that is considered to be acceptable accuracy. Histogram analysis in **Fig. 14** (d) demonstrates the percentage of the elements with certain error range for the right-hand side of the L-wall structure. It can be seen that approximately 2.5 % of the elements exhibit error values greater than 10 % by using the novel integrated ANN-FE approach.

5.3. 18-layers rectangular box

Fig. 15 shows the stress results obtained from the FE analysis and the novel integrated ANN-FE method for the 18-layers rectangular box. **Fig. 15** (a) and (b) demonstrate the S_{11} (stress component in direction 1) obtained from the detailed finite element analysis and integrated ANN-FE approach, respectively. As it is depicted, the overall residual stress distribution and its pattern are consistent in both contours especially in the top layer and the bottom of the box where the positive residual stresses are high. The error scatter is evaluated for the outer surface of the shown side in **Fig. 15** (c) in 3D space. By evaluating the prediction error from the ANN-FE method, it can be concluded that the significant number of elements show the error values less than 3.5 % which is shown in **Fig. 15** (c). The high error values, approximately 25–30 %, corresponds to the very limited number of elements located on the top surface of the 18th layer shown in **Fig. 15** (c). The error scatter in **Fig. 15** (d) shows that the high volume of elements shows lower than 15 %

considering the complexity of the box structure. By assessing the histogram analysis for the elements, it is seen that approximately 5 % of the elements on the surface of the shown side have error values higher than 15 %. The employed integrated ANN-FE method show a high capability of predicting the residual stresses in the rectangular box.

Fig. 16 shows the S_{22} distribution (stress component in the stacking direction or direction 2) for the rectangular box structure. **Fig. 16** (a) and (b) show the S_{22} obtained from FE analysis and the novel integrated ANN-FE approach, respectively. The distribution pattern in both cases is consistent and the high tensile and compressive residual stresses are captured well in the ANN-FE approach. The S_{22} distribution over the whole medium is smooth. The corners show tensile residual stresses followed by a smooth transition to compressive residual stresses in the middle of the part. Higher compressive stresses are observed in the inner side of the box and the prediction made from the integrated ANN-FE approach is in good agreement with the results of the detailed FE analysis. The error scatter analysis represented in **Fig. 16** (c) and (d), indicates that that the number of elements with the error greater than 15 % is limited. Histogram error analysis of S_{11} error is shown in **Fig. 16** (d). Only 5 % of the elements show the prediction error higher than 15 %. As mentioned before, a high fraction of elements has a low prediction error as it is supported by the histogram analysis.

A summary of the error analysis for the three structural parts considered in the present study is provided in **Table 4**. It is shown that the prediction obtained for the 18-layers L-wall is more accurate than the other two parts. Although the box has more complex geometric features than the straight wall, the percentage of the elements with higher prediction error than 15 % is greater than of the straight wall. The training step of implementing the ANN-FE approach should be repeated until the better performance of the ANN be achieved. This may be the main drawback of employing ANN for prediction purposes. This can be improved by applying the proposed modeling approach to different structural parts with distinct configurations and achieving a better perception of ML algorithms.

The training time of the ANN is different for every structure based on the size of the dataset, number of the hidden layers, number of neurons in each layer of the network, and number of the epochs for training the network. The computational time of the FE-based model and the ANN-FE model for three different structural parts are shown in **Table 5**. By comparing the computational time of the thermo-mechanical FE analysis and the novel ANN-FE integrated approach for every part, it is evident that the computational time for all the three structural parts studied has improved significantly. As seen from **Table 5**, the computational times have been improved by 4.3 times for the 18-layers wall, 5.3 times for the 18-layers L-shape wall, and 6.1 times for the 18-layers rectangular box. It should be noted that the computational time of the novel ANN-FE integrated model is governed by the training time of the ANNs. However, once the network is trained, it can be used for any type of predictions regarding the study of the effect of process parameters on the residual distribution of the DMD fabricated part with the same geometry. In other words, for any combination of the process parameters, a simple pure heat transfer analysis is performed to obtain the temperature history of the elements, then, it will be fed into the trained network to predict the residual stress distribution of the DMD part. Therefore, the computational time will be significantly lower since there is no need for training the network anymore. Furthermore, by comparing the improvement in computational times of the novel proposed approach for the three structures, the more complex structure i.e. 18-layers rectangular box indicates a higher improvement rate in the computational time. This means the integrated ANN-FE approach is most beneficial for complex shapes with a higher number of elements which makes the thermo-mechanical FE analysis more time-consuming. Furthermore, the part thickness plays an important role in the residual stress distribution of AM structural parts [57,58]. The integrated ANN-FE modeling framework offers to have a high potential solution for analyzing thickness effects in the stress distribution of DED parts. Therefore, as a future

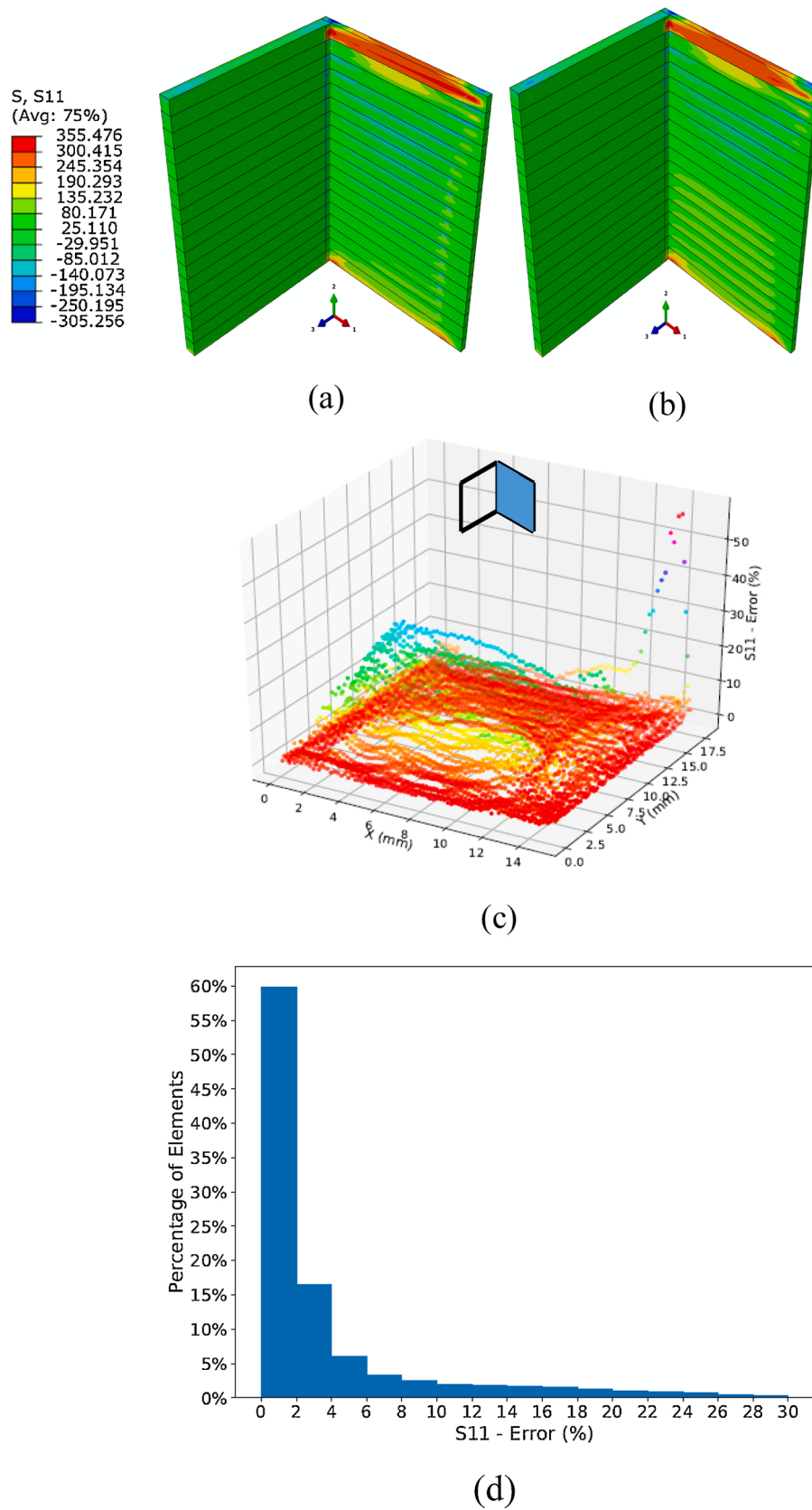


Fig. 13. S₁₁ distribution of 18-layers L-wall (in MPa) (a) FEM analysis (b) integrated ANN-FE (c) 3D error scatter of the right side (d) histogram of the error.

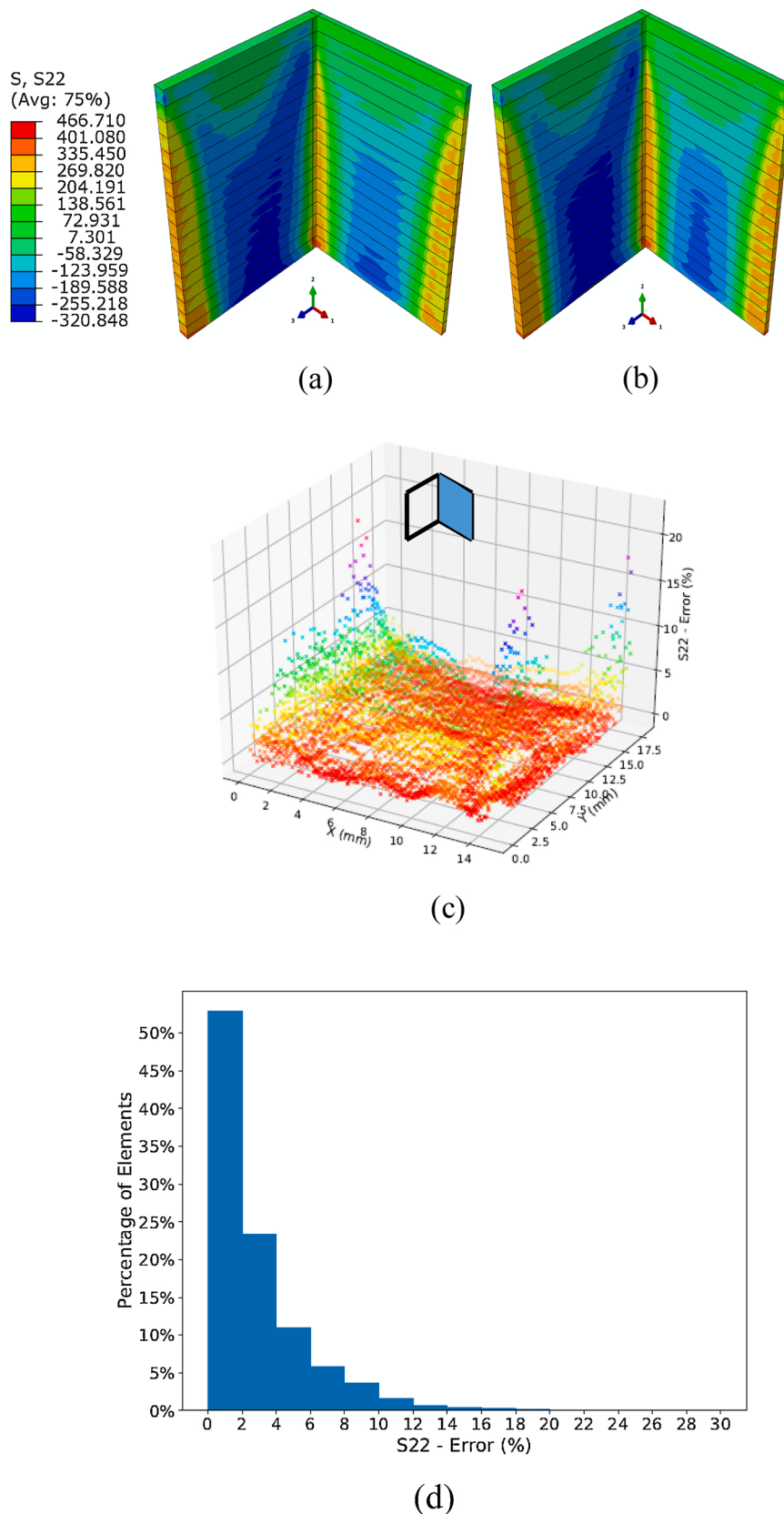


Fig. 14. S_{22} distribution of 18-layers L-wall (in MPa) (a) FEM analysis (b) ANN prediction (c) 3D error scatter (d) histogram of the error.

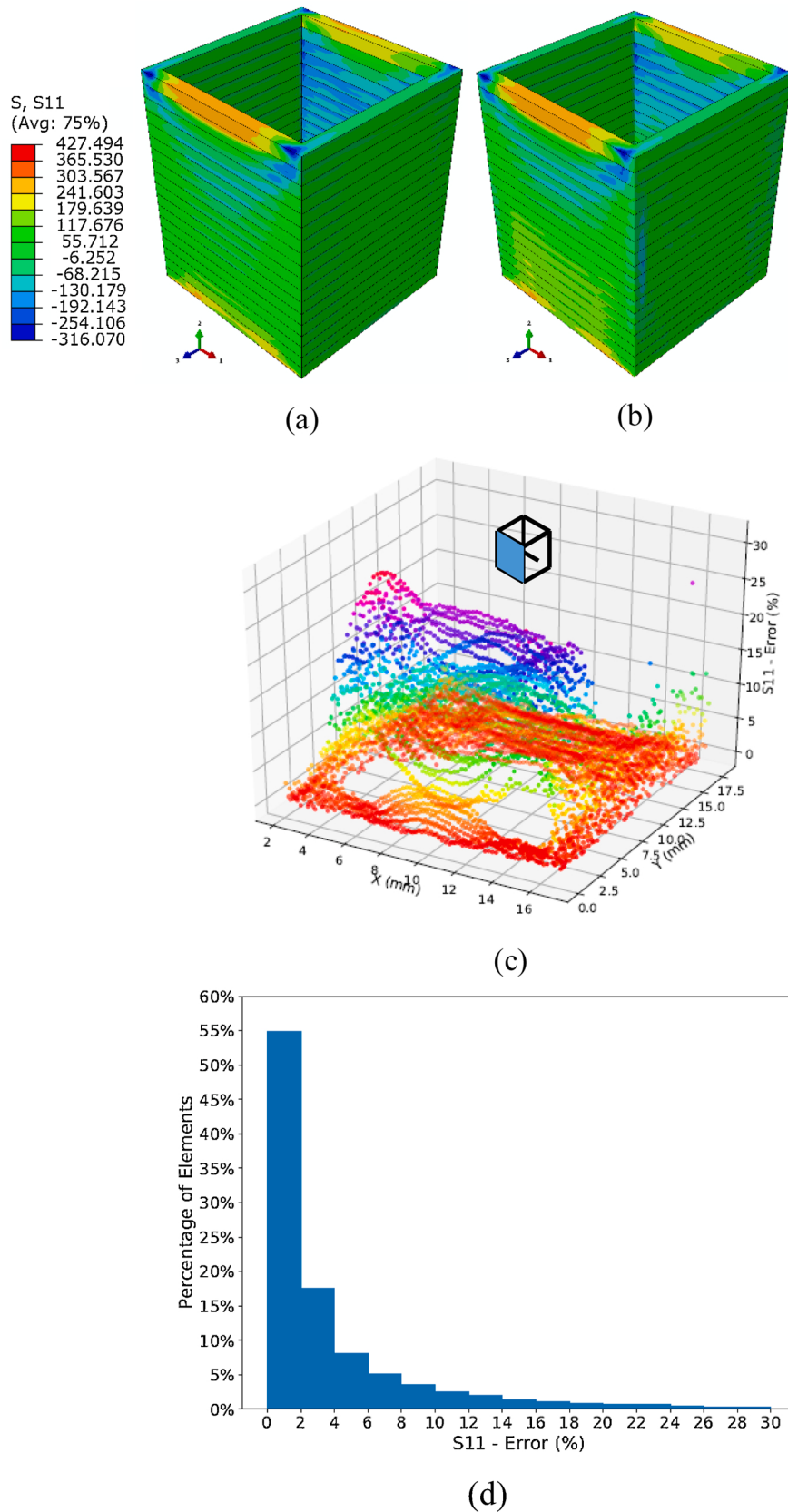


Fig. 15. S₁₁ distribution of 18-layers rectangular box (in MPa) (a) FEM analysis (b) ANN prediction (c) 3D error scatter (d) histogram of the error.

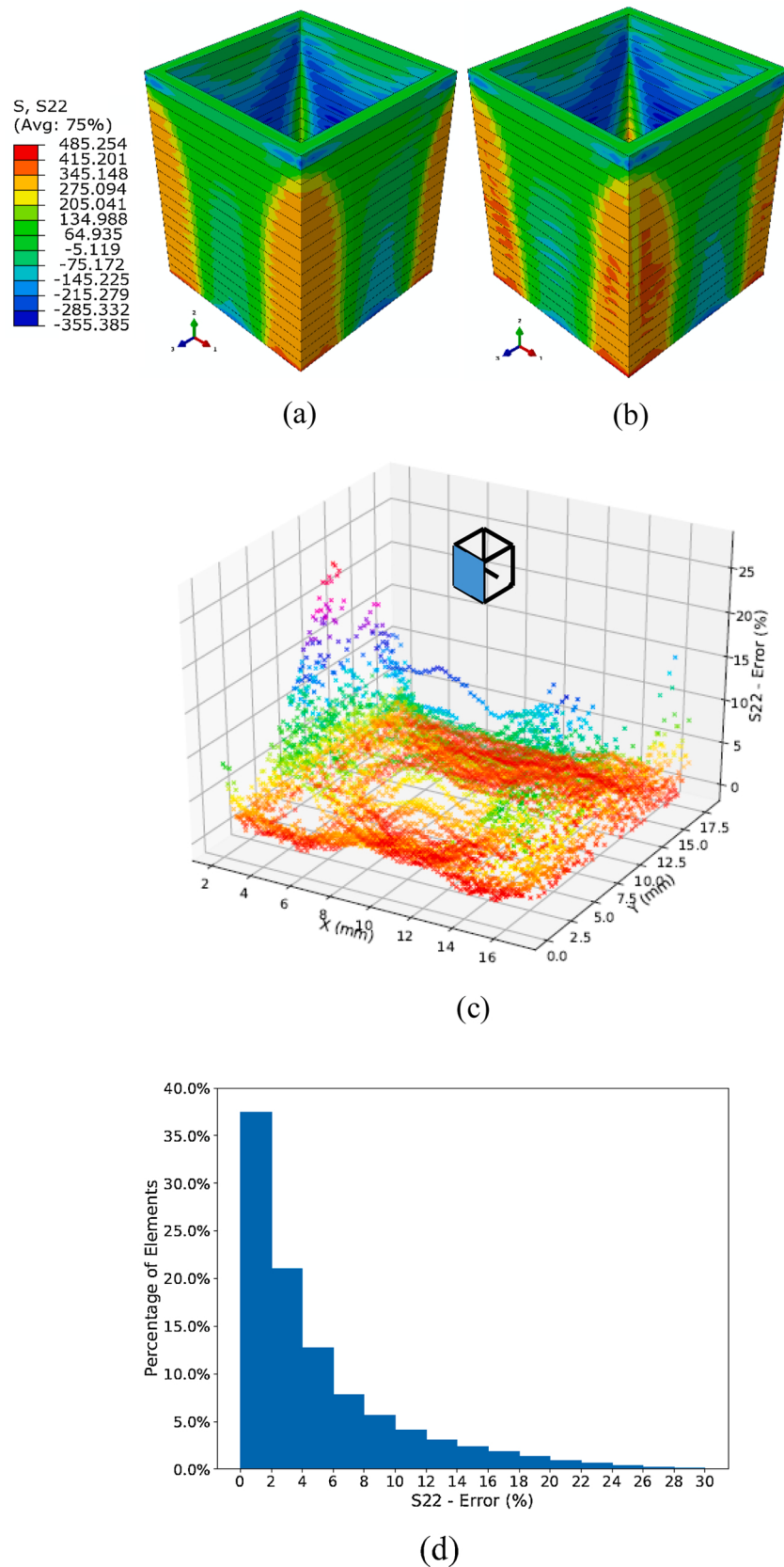


Fig. 16. S_{22} distribution of 18-layers rectangular box (in MPa) (a) FEM analysis (b) ANN prediction (c) 3D error scatter (d) histogram of the error.

Table 4

Percentage of elements in each structure with the prediction error higher than 15 %.

	Stress	18-layers wall	18-layers L-wall	18-layers rectangular box
Percentage of elements	S_{11}	12 %	2 %	5 %
	S_{22}	3 %	1 %	5 %

Table 5

Comparison of computational time between FE-based model and ANN-FE model.

Structure	18-layers wall	18-layers L-wall	18-layers rectangular box	
Run time	FE analysis Integrated ANN-FE	26 h 6 h	69 h 12 h	128 h 20 h

work, the present researchers are encouraged to investigate residual stresses of more complex structures with varying thickness by applying the proposed novel approach.

6. Conclusion

A novel modeling approach for integrating ANN with the FE analysis is developed in order to provide the efficient and accurate prediction of the residual stress distribution of DMD parts. The proposed approach is implemented for three simple structures including 12-layers and 18-layers wall, L-shape, and rectangular box. The most valuable outcomes of the present study are listed in the following:

- The predicted residual stress results of the thermo-mechanical FE analysis and the results obtained from the novel integrated ANN-FE approach on the three structures are in good agreement.
- The ANN algorithms show the promising capability for prediction and evaluation of residual stresses of AM structural parts.
- A very limited number of elements showed the prediction error higher than 15 %. For the cases considered in the present study, the 18-layers L-wall showed more accurate results than the other two structures; the percentage of elements with the prediction error higher than 15 % was approximately 2 % and 1 % for S_{11} and S_{22} , respectively.
- The computational time for predicting the residual stresses improved by a factor of 4.3, 5.3, and 6.1 times for 18-layers wall, 18-layers L-shape wall, and 18-layers rectangular box using the novel ANN-FE integrated model, respectively.
- The integrated ANN-FE can offer significant improvement in the computational time of predicting the residual stress distribution of complex structures fabricated by DMD process.

It is suggested that further research work needs to focus on more complex geometrical structures with varying thicknesses to test and improve simulation capability of the proposed novel modeling approach.

Data availability

The raw/processed data required to reproduce these findings cannot be shared at this time due to technical or time limitations, but it will be provided upon request.

CRediT authorship contribution statement

F. Hajializadeh: Methodology, Software, Data curation, Writing - original draft, Validation. **A. Ince:** Conceptualization, Supervision, Writing - review & editing.

Declaration of Competing Interest

The authors declare that they have no known competing financial interests or personal relationships that could have appeared to influence the work reported in this paper.

Acknowledgements

The authors would like to acknowledge the financial support of Natural Sciences and Engineering Research Council of Canada (NSERC) (DGECR-2018-00232).

References

- L. Sun, X. Ren, J. He, J.S. Olsen, S. Pallaspuro, Z. Zhang, A new method to estimate the residual stresses in additive manufacturing characterized by point heat source, *Int. J. Adv. Manuf. Technol.* 105 (2019) 2415–2429.
- G. Piscopo, E. Atzeni, A. Salmi, A hybrid modeling of the physics-driven evolution of material addition and track generation in laser powder directed energy deposition, *Materials* 12 (2019) 2819.
- J. Ning, E. Mirkoohi, Y. Dong, D.E. Sievers, H. Garmestani, S.Y. Liang, Analytical modeling of 3D temperature distribution in selective laser melting of Ti-6Al-4V considering part boundary conditions, *J. Manuf. Process.* 44 (2019) 319–326.
- I. van Hengel, N. Putra, M. Tierolf, M. Minneboo, A. Fluit, L. Fratila-Apacitei, et al., Biofunctionalization of selective laser melted porous titanium using silver and zinc nanoparticles to prevent infections by antibiotic-resistant bacteria, *Acta Biomater.* (2020).
- I. Konyashin, H. Hinnens, B. Ries, A. Kirchner, B. Klöden, B. Kieback, et al., Additive manufacturing of WC-13% Co by selective electron beam melting: achievements and challenges, *Int. J. Refract. Metals Hard Mater.* 84 (2019), 105028.
- M.I. Al Hamahmy, I. Deib, Review and analysis of heat source models for additive manufacturing, *Int. J. Adv. Manuf. Technol.* 106 (2020) 1223–1238.
- A. Nycz, V. Kishore, J. Lindahl, C. Duty, C. Carnal, V. Kunc, Controlling substrate temperature with infrared heating to improve mechanical properties of large-scale printed parts, *Addit. Manuf.* 33 (2020), 101068.
- B.E. Carroll, T.A. Palmer, A.M. Beese, Anisotropic tensile behavior of Ti-6Al-4V components fabricated with directed energy deposition additive manufacturing, *Acta Mater.* 87 (2015) 309–320.
- L.E. Murr, S.M. Gaytan, D.A. Ramirez, E. Martinez, J. Hernandez, K.N. Amato, et al., Metal fabrication by additive manufacturing using laser and electron beam melting technologies, *J. Mater. Sci. Technol.* 28 (2012) 1–14.
- S. Ashley, Rapid prototyping systems, *Mech. Eng.* 113 (1991) 34.
- J.-P. Kruth, M.-C. Leu, T. Nakagawa, Progress in additive manufacturing and rapid prototyping, *CIRP Ann. Manuf. Technol.* 47 (1998) 525–540.
- K.V. Wong, A. Hernandez, A review of additive manufacturing, *ISRN Mech. Eng.* 2012 (2012).
- X. Liang, L. Cheng, Q. Chen, Q. Yang, A.C. To, A modified method for estimating inherent strains from detailed process simulation for fast residual distortion prediction of single-walled structures fabricated by directed energy deposition, *Addit. Manuf.* 23 (2018) 471–486.
- T. Mukherjee, W. Zhang, T. DebRoy, An improved prediction of residual stresses and distortion in additive manufacturing, *Comput. Mater. Sci.* 126 (2017) 360–372.
- S.-P. Zhu, Q. Liu, W. Peng, X.-C. Zhang, Computational-experimental approaches for fatigue reliability assessment of turbine bladed disks, *Int. J. Mech. Sci.* 142 (2018) 502–517.
- S.-P. Zhu, D. Liao, B. Keshtgar, G. Qian, Q. Wang, Probabilistic framework for fatigue life assessment of notched components under size effects, *Int. J. Mech. Sci.* 181 (2020), 105685.
- P. Ferro, F. Berto, M.N. James, Asymptotic residual stresses in butt-welded joints under fatigue loading, *Theor. Appl. Fract. Mech.* 83 (2016) 114–124.
- J. Zheng, A. Ince, L. Tang, Modeling and simulation of weld residual stresses and ultrasonic impact treatment of welded joints, *Procedia Eng.* 213 (2018) 36–47.
- L. Tang, A. Ince, J. Zheng, Numerical modeling of residual stresses and fatigue damage assessment of ultrasonic impact treated 304L stainless steel welded joints, *Eng. Fail. Anal.* 108 (2020), 104277.
- B.K. Panda, S. Sahoo, Thermo-mechanical modeling and validation of stress field during laser powder bed fusion of AlSi10Mg built part, *Results Phys.* 12 (2019) 1372–1381.
- G.R. Nazami, B.K. Panda, S. Sahoo, Finite element simulation of residual stress in direct metal laser sintering of AlSi10Mg built part: effect of laser spot overlapping, *Materials Today: Proceedings* (2020).
- S. Jayanath, A. Achuthan, A computationally efficient finite element framework to simulate additive manufacturing processes, *J. Manuf. Sci. Eng.* 140 (2018), 041009.
- F. Hajializadeh, A. Ince, Finite element based numerical modeling framework for additive manufacturing process, *Mat. Des. Process Comm.* (2019) 1–7.
- N. Keller, V. Plosikhin, New Method for Fast Predictions of Residual Stress and Distortion of AM Parts. Solid Freeform Fabrication Symposium (SFF), Austin, TX, Aug, 2014, pp. 4–6.
- L.A. Parry, Investigation of Residual Stress in Selective Laser Melting, University of Nottingham, 2018.

- [26] M. Bugatti, Q. Semeraro, Limitations of the inherent strain method in simulating powder bed fusion processes, *Addit. Manuf.* (2018).
- [27] Y. Ueda, Y.C. Kim, M.G. Yuan, A predicting method of welding residual stress using source of residual stress (report I): characteristics of inherent strain (source of residual stress)(mechanics, strength & structural design), *Trans. JWRI* 18 (1989) 135–141.
- [28] S.-P. Zhu, B. Keshtegar, M. Bagheri, P. Hao, N.-T. Trung, Novel hybrid robust method for uncertain reliability analysis using finite conjugate map, *Comput. Methods Appl. Mech. Eng.* 371 (2020), 113309.
- [29] A. Koeppe, C.A.H. Padilla, M. Voshage, J.H. Schleifenbaum, B. Markert, Efficient numerical modeling of 3D-printed lattice-cell structures using neural networks, *Manuf. Lett.* 15 (2018) 147–150.
- [30] L. Liang, M. Liu, C. Martin, W. Sun, A deep learning approach to estimate stress distribution: a fast and accurate surrogate of finite-element analysis, *J. R. Soc. Interface* 15 (2018), 20170844.
- [31] T. Gulikers, An Integrated Machine Learning and Finite Element Analysis Framework, Applied to Composite Substructures Including Damage, 2018.
- [32] S. Chowdhury, S. Anand, Artificial neural network based geometric compensation for thermal deformation in additive manufacturing processes, International Manufacturing Science and Engineering Conference: American Society of Mechanical Engineers (2016) V003T08A6.
- [33] Z. Li, Z. Zhang, J. Shi, D. Wu, Prediction of surface roughness in extrusion-based additive manufacturing with machine learning, *Robot. Comput. Manuf.* 57 (2019) 488–495.
- [34] S.N.S. Mortazavi, A. Ince, An artificial neural network modeling approach for short and long fatigue crack propagation, *Comput. Mater. Sci.* (2020) 185.
- [35] Y. Yang, M. Jamshidinia, P. Boulware, S. Kelly, Prediction of microstructure, residual stress, and deformation in laser powder bed fusion process, *Comput. Mech.* (2018) 1–17.
- [36] N. Raghavan, R. Dehoff, S. Pannala, S. Simunovic, M. Kirka, J. Turner, et al., Numerical modeling of heat-transfer and the influence of process parameters on tailoring the grain morphology of IN718 in electron beam additive manufacturing, *Acta Mater.* 112 (2016) 303–314.
- [37] P. Michaleris, Modeling metal deposition in heat transfer analyses of additive manufacturing processes, *Finite Elem. Anal. Des.* 86 (2014) 51–60.
- [38] E.R. Denlinger, J.C. Heigel, P. Michaleris, Residual stress and distortion modeling of electron beam direct manufacturing Ti-6Al-4V, *Proc. Inst. Mech. Eng. Part B: J. Eng. Manuf.* 229 (2015) 1803–1813.
- [39] L. Yan, Y. Zhang, F. Liou, A conceptual design of residual stress reduction with multiple shape laser beams in direct laser deposition, *Finite Elem. Anal. Des.* 144 (2018) 30–37.
- [40] J. Song, J. Shanghvi, P. Michaleris, Sensitivity analysis and optimization of thermo-elasto-plastic processes with applications to welding side heater design, *Comput. Methods Appl. Mech. Eng.* 193 (2004) 4541–4566.
- [41] G. Fu, J. Gu, M.I. Lourenco, M. Duan, S.F. Esteve, Parameter determination of double-ellipsoidal heat source model and its application in the multi-pass welding process, *Ships Offshore Struct.* 10 (2015) 204–217.
- [42] A. Lundbäck, Finite Element Modelling and Simulation of Welding of Aerospace Components, Luleå tekniska universitet, 2003.
- [43] A. Vasinonta, J.L. Beuth, M. Griffith, Process maps for predicting residual stress and melt pool size in the laser-based fabrication of thin-walled structures, *J. Manuf. Sci. Eng.* 129 (2007) 101–109.
- [44] S. Ghosh, J. Choi, Three-dimensional transient finite element analysis for residual stresses in the laser aided direct metal/material deposition process, *J. Laser Appl.* 17 (2005) 144–158.
- [45] S. Bontha, N.W. Klingbeil, Effect of a distributed heat source on melt pool geometry and microstructure in beam-based solid freeform fabrication, in: Proceedings 2006 Solid Freeform Fabrication Symposium, Austin, TX, 2006.
- [46] J. Goldak, A. Chakravarti, M. Bibby, A new finite element model for welding heat sources, *Metall. Trans. B* 15 (1984) 299–305.
- [47] L. Svensson, B. Gretoft, H. Bhadeshia, An analysis of cooling curves from the fusion zone of steel weld deposits, *Scand. J. Metall.* 15 (1986) e103.
- [48] V. Manvatkar, A. De, T. DebRoy, Heat transfer and material flow during laser assisted multi-layer additive manufacturing, *J. Appl. Phys.* 116 (2014), 124905.
- [49] F. Hajializadeh, A. Ince, Short review on modeling approaches for metal additive manufacturing process, *Mater. Des. Proc. Commun.* 2 (2020) e56.
- [50] Q. Yang, P. Zhang, L. Cheng, Z. Min, M. Chyu, A.C. To, Finite element modeling and validation of thermomechanical behavior of Ti-6Al-4V in directed energy deposition additive manufacturing, *Addit. Manuf.* 12 (2016) 169–177.
- [51] E.R. Denlinger, J. Irwin, P. Michaleris, Thermomechanical modeling of additive manufacturing large parts, *J. Manuf. Sci. Eng.* 136 (2014), 061007.
- [52] R.I. Borja, Plasticity, Springer, 2013.
- [53] F. Rosenblatt, Principles of Neurodynamics. Perceptrons and the Theory of Brain Mechanisms, Cornell Aeronautical Lab Inc, Buffalo NY, 1961.
- [54] N. Ketkar, Introduction to Keras. Deep Learning With Python, Springer, 2017, pp. 97–111.
- [55] G. Cybenko, Approximation by superpositions of a sigmoidal function, *Math. Control. Signals Syst.* 2 (1989) 303–314.
- [56] C.C. Aggarwal, Neural Networks and Deep Learning, Springer, 2018.
- [57] F. Berto, P. Lazzarin, A. Kotousov, On higher order terms and out-of-plane singular mode, *Mech. Mater.* 43 (2011) 332–341.
- [58] L. Pook, A. Campagnolo, F. Berto, Coupled fracture modes of discs and plates under anti-plane loading and a disc under in-plane shear loading, *Fatigue Fract. Eng. Mater. Struct.* 39 (2016) 924–938.